Bulletin of Volcanology

Constraining pre-eruptive magma conditions and unrest timescales during the Monte Nuovo eruption (Campi Flegrei, Southern Italy): integrating textural and CSD results for experimental and natural trachy-phonolites

--Manuscript Draft--

Manuscript Number:	
Full Title:	Constraining pre-eruptive magma conditions and unrest timescales during the Monte Nuovo eruption (Campi Flegrei, Southern Italy): integrating textural and CSD results for experimental and natural trachy-phonolites
Article Type:	Research Article
Corresponding Author:	Fabio Arzilli, Ph.D. University of Manchester Manchester, UNITED KINGDOM
Corresponding Author Secondary Information:	
Order of Authors:	Fabio Arzilli, Ph.D.
	Monica Piochi
	Angela Mormone
	Claudia Agostini
	Michael R. Carroll
Funding Information:	2005–2006 INGV-DPC project V3-2/UR14 — Dr Monica Piochi
	FAR 2012 — Prof. Michael R. Carroll
Abstract:	We present crystallization experiments concerning a broad range of growth conditions of alkali feldspar and sodalite in trachy-phonolite magma composition during their later evolution state. Our results include: i) textural data and mineral assemblage of synthetic samples, ii) feldspar kinetics and growth rate estimates, and iii) textural data, mineral abundances and Crystal Size Distribution trend of samples representative of the Monte Nuovo eruption (1538 AD, last in the Campi Flegrei, Southern Italy). Experiments reproduced the texture and feldspar content of natural products indicating that the kinetics data can provide insights into processes within the volcanic system shortly before and during this small-magnitude eruption, and, particularly, about magma ascent timescale. Based on the bulk of the results we suggest that the groundmass crystallization of Monte Nuovo magma started between 7 and 4 km of depth (≤200 MPa) at a temperature between 825 and 840 °C (close to the liquidus of alkali feldspar). The crystallization kinetics of alkali feldspar and the absence of sodalite in most of the natural samples indicate that the magma ascent was faster between 2 and 3 km (50-70 MPa) before to reach the fragmentation zone, during the first phases of the eruption. The crystallization time of the magma allows us to definitively constrain that the magma reached the fragmentation level in few days to several hours. Here we also show that a small decrease in pressure could induce a dramatic increase of crystallinity with associated rheological changes able to modify the eruption style. Thus, the products from the later phases of the Monte Nuovo eruption are more crystalline and contain sodalite in response to the reaching a shallower fragmentation depth.
Suggested Reviewers:	Caroline Martel caroline.martel@cnrs-orleans.fr
	Francesco Vetere francesco.vetere@unipg.it
	Luca Caricchi luca.caricchi@unige.ch
	Christopher R. J. Kilburn

	c.kilburn@ucl.ac.uk
	Malcolm J. Rutherford Malcolm_Rutherford@Brown.EDU

Constraining pre-eruptive magma conditions and unrest timescales during the Monte Nuovo eruption (Campi Flegrei, Southern Italy): integrating textural and CSD results for experimental and natural trachy-phonolites

Fabio Arzilli[ab*], Monica Piochi[c], Angela Mormone[c], Claudia Agostini[b], Michael R. Carroll[b]

[a] School of Earth, Atmospheric and Environmental Sciences, The University of Manchester, Oxford Road, Manchester, M13 9PL, UK

[b]School of Science and Technology - Geology Division, University of Camerino, Via Gentile III da Varano, 62032 Camerino, Italy

[c]Istituto Nazionale di Geofisica e Vulcanologia, sezione Osservatorio Vesuviano, Via Diocleziano 328, 80124 Napoli, Italy

[*]Corresponding author: Dr. Fabio Arzilli

Corresponding author present affiliation: School of Earth, Atmospheric and Environmental Sciences, The University of Manchester, Oxford Road, Manchester, M13 9PL, UK

E-mail address: arzilli.fabio@gmail.com

Phone: +393298429732

Abstract

We present crystallization experiments concerning a broad range of growth conditions of alkali feldspar and sodalite in trachy-phonolite magma composition during their later evolution state. Our results include: i) textural data and mineral assemblage of synthetic samples, ii) feldspar kinetics and growth rate estimates, and iii) textural data, mineral abundances and Crystal Size Distribution trend of samples representative of the Monte Nuovo eruption (1538 AD, last in the Campi Flegrei, Southern Italy). Experiments reproduced the texture and feldspar content of natural products indicating that the kinetics data can provide insights into processes within the volcanic system shortly before and during this small-magnitude eruption, and, particularly, about magma ascent timescale. Based on the bulk of the results we suggest that the groundmass crystallization of Monte Nuovo magma started between 7 and 4 km of depth (≤200 MPa) at a temperature between 825 and 840 °C (close to the liquidus of alkali feldspar). The crystallization kinetics of alkali feldspar and the absence of sodalite in most of the natural samples indicate that the magma ascent was faster between 2 and 3 km (50-70 MPa) before to reach the fragmentation zone, during the first phases of the eruption. The crystallization time of the magma allows us to definitively constrain that the magma reached the fragmentation level in few days to several hours. Here we also show that a small decrease in pressure could induce a dramatic increase of crystallinity with associated rheological changes able to modify the eruption style. Thus, the products from the later phases of the Monte Nuovo eruption are more crystalline and contain sodalite in response to the reaching a shallower fragmentation depth.

Keywords: alkali feldspars; trachytic melts; crystallization kinetics; CSD; Monte Nuovo; Campi Flegrei

1. Introduction

1.1 The aim of the study

Alkali feldspar is an abundant crystal phase in evolved alkaline rocks (phonolites, alkali rhyolites), and is widespread in the Campania Province (Piochi et al. 2005). Its occurrence as microlites in the pumice and scoria groundmass potentially provides information on the timescale of magma migration within the crust, specifically from the magma chamber to the fragmentation level (Marsh 1988; Cashman and Marsh 1988; Marsh 1998). This information may be unraveled by studying the size distribution of microlites pre- and syn-eruptively crystallized and quenched in the matrix of juvenile fragments. Since the crystals present in an igneous rock and the observed variations in both their composition and texture reflect the integrated pressure (P) - temperature (T) - composition (X) - time (t) history of the magma from which they formed, it is possible to link textural observations with experimentally derived data for rates of crystal growth (Y_L) and crystal number density (N_a) for the specific mineral phase and the undercooling (ΔT) values of the parental melt. In fact, this allows us to gain insights into magmatic processes and their time-scales using textural observation.

However, there are few studies about crystallization kinetics on trachy-phonolitic melts (e.g., Iezzi et al. 2008; Arzilli and Carroll 2013). In this study we present results for 16 new crystallization experiments on hydrous trachytic melt, which complement the previous experimental work of Arzilli and Carroll (2013). All of the experiments use the same single-step (cooling and decompression) method to reproduce the trachytic melt evolution in response to instantaneously applied thermodynamic driving force (i.e., undercooling, $\Delta T = T_{liquidus} - T_{experimental}$).

The experiments were conducted at different pressures and ΔT, in order to highlight the differences in crystallinity between high and low pressure (and thus melt H_2O content). The preliminary study of Arzilli and Carroll (2013) focused mainly on the influence of ΔT and time on the nucleation and growth of alkali feldspar. They showed the occurrence of several nucleation events of alkali feldspar in short times (hours), with dominance of nucleation at large ΔT. Here we utilize our

experiments and those performed by Arzilli and Carroll (2013) to study how the crystallization may change as a function of P_{H2O} (proportional to melt water content for the water-saturated conditions investigated) and ΔT (induced by cooling and/or decompression). Our study is focused in understanding how fast the crystallinity of a trachytic magma could change after small variation of pressure. These experiments provide constraints on the P-T conditions of the trachytic to phonolitic melts during their ascent to the surface. Therefore, differently from Arzilli and Carroll (2013), here we use the experiments to better understand the volcanological and magmatic processes during the Monte Nuovo eruption in the Campi Flegrei (Southern Italy; Fig. 1). This eruption is particularly interesting because it occurred after 3000 years of volcanic quiescence and following a period of ground level movements and seismicity with characteristics comparable to the recent bradyseisms in the Campi Flegrei area (Parascandola 1947; Del Gaudio et al. 2010), as described by historical chronicles (Guidoboni and Ciucciarelli 2011). Constraining the timing of magma movements in the subsurface shortly before the eruption is crucial to unravel the significance of phenomena affecting the Campi Flegrei during volcanic quiescence. The eruption was already the object of similar studies (D'Oriano et al. 2005; Piochi et al. 2005) that, nevertheless, were limited by the lack of crystallization kinetic data for trachytic-phonolitic melt compositions (D'Oriano et al. 2005; Piochi et al. 2005). In order to constrain the conditions and the timescales of magmatic processes, we focus on the crystallization kinetics of alkali feldspar in trachytic melts and new crystal size distribution (CSD) data for groundmass feldspars in the natural samples. This choice is in line with several studies (e.g. Geschwind and Rutherford 1995; Hammer and Rutherford 2002; Couch et al. 2003; Armienti et al. 2007; Martel 2012) that used crystallization kinetics and CSD of feldspar (mainly plagioclase) to unravel shallow dynamics in pre- and syn-eruptive conditions at several calc-alkaline volcanoes; our new data allow similar investigation using the abundant alkali feldspar crystals in the Campi Flegrei system (e.g., Piochi et al. 2005; 2008 and reference therein).

1.2 Volcanological and petrological background

The 1538 Monte Nuovo eruption (Fig. 1a-e) was characterized by relatively low intensity and magnitude (Di Vito et al. 1987; D'Oriano et al. 2005; Piochi et al. 2005, 2008). Similar to the majority of volcanic eruptions of the last 14.9 ka b.p. in the area (see Rosi et al. 1983; Di Vito et al. 1999; Isaia et al. 2009), it occurred from a monogenic vent and extruded <0.1 km^3 of magma (Lirer et al. 1987; Rosi and Sbrana 1987; Mormone et al. 2011; Smith et al. 2011) with a K-rich, phono-trachytic composition (Fig. 2) that generated sparsely porphyritic magmas, with typically alkaline feldspars, and variably vesicular pumice and scoria fragments (e.g., Rosi and Sbrana 1987; Piochi et al. 2008; D'Oriano et al. 2005). However, the Monte Nuovo eruption seems to be an exceptional event in the Campi Flegrei history, given that in the past 14.9 ka Campi Flegrei volcanism mostly concentrated in epochs of intense activity, alternating with quiescence periods of thousands of years; in such epochs eruptions occurred with a decadal frequency (Di Renzo et al. 2011; Smith et al. 2011). Instead, the Monte Nuovo event was the last and occurred after a volcanic quietness of ~3000 years.

The eruption occurred in an area characterized by persistent fumarolic activity and by bradyseisms since AD 1450 (Parascandola 1947; Lirer et al. 1987; Guidoboni and Ciucciarelli 2011) (Fig. 1d). Uplift episodes (bradyseisms) occurred in 1503 and 1511 AD (Fig. 1d) inducing the local Authorities to work on the reconstruction of earthquake damaged buildings and to establish the ownership of the new land created. However, strong and continuous seismicity was described since the middle of AD 1536 with a significant progressive intensification about 3 months before the eruption (see table 2 in Guidoboni and Ciucciarelli 2011; see also Fig. 1d,e). In the middle of September, 1536, the ground deformations focused in a small zone where a vent opened along the coastal sector of the Averno Lake (Fig. 1a). Up to 4.5 meters of uplift occurred 1 day before the eruption, with the sea recession of about 400 m. Fractures at the surface with hot groundwater outflow, flames, and sudden uplift of a sunken area preceded the explosion of smoke and incandescent material that destroyed Le Tripergole Village. The eruption started in the night between September 29th and 30th (Guidoboni and Ciucciarelli 2011) and the first phreato-magmatic

128 phase produced pumiceous lapilli-bearing ash deposits that built the cone, whereas the final activity
129 generated scoria deposits. The first main deposit (LM in D'Oriano et al. 2005, and Unit I-II in Di
130 Vito et al. 1987) is composed of coarse to fine ash levels, being coarser-sized and lapilli-bearing in
131 the lowermost levels (Unit I) where they are intercalated with pumice or scoria lenses or beds
132 (Boivin et al. 1982). Block sags are common, while juvenile fragments are often sub-rounded,
133 associated to infrequent obsidian-like clasts and lava and tuff lithics. This deposit was emplaced by
134 pyroclastic flow mechanism. On October 3, after two days of diminishing violence, explosions
135 produced two dark scoriae layers intercalated with a gray ash bed (UM1 or Unit III, in D'Oriano et
136 al. 2005 and Di Vito et al. 1987, respectively). The final phase, after 3 days of eruptive quiescence,
137 produced a scoria unit by flow (UM2 in D'Oriano et al. 2005) or/and fallout (Unit IV in Di Vito et
138 al. 1987) mechanism.
139
140 2. Methods: synthetic and natural products
141 2.1 Synthetic products: starting material and experimental strategy
142 We complete the experiments of Arzilli and Carroll (2013) to obtain a wider data set of feldspar
143 crystallization conditions involving growth under cooling, decompression and
144 "cooling+decompression" experiments. The starting material (Table 1) is the same obsidian used in
145 previous runs; it was sampled within the Breccia Museo Unit, a pyroclastic breccia associated with
146 the Campanian Ignimbrite eruption dated at c.a 39 ka (Melluso et al. 1995; Fedele et al. 2008). The
147 sample is known as ZAC in the literature (Di Matteo et al. 2004; Fabbrizio and Carroll 2008;
148 Calzolaio et al. 2010; Arzilli and Carroll 2013). It is sub-aphiric with <10% by volume of crystals.
149 Phenocrysts are mostly alkali feldspar with minor plagioclase, clinopyroxene, biotite and magnetite,
150 in order of decreasing abundance; apatite and titanite are accessory phases. The composition is
151 trachytic, near the trachyte-phonolite border in the TAS diagram (Di Matteo et al. 2004). It is
152 similar but not identical to the Monte Nuovo products in terms of whole-rock and glassy matrix
153 chemistry (Fig. 2; Table 1); also it presents slight differences for content of phenocrysts (<10%

154 ZAC vs. 3% Monte Nuovo) and mineral assemblage (much abundance of pyroxene and biotite in
155 ZAC). Despite these small differences, we use ZAC for which the phase diagram (Fabbrizio and
156 Carroll 2008; Arzilli and Carroll 2013) allowed us to choose accurately the experimental conditions
157 relevant for our study the feldspar crystallization kinetic. Also, Piochi et al. (2008) proposed similar
158 composition for the magma systems feeding eruptions at the Campi Flegrei.
159 To complete the experimental data set of Arzilli and Carroll (2013), we have performed 16 new
160 crystallization experiments. Particularly, we extend cooling and degassing experiments in water-
161 saturated conditions towards higher pressure (experimental final pressure, P_f = 100, 150 and 200
162 MPa) and lower pressure (P_f = 30 and 50 MPa) within a range of temperatures between 750 and 850
163 °C (Table 2). The initial conditions of the experiments were above the liquidus of the alkali
164 feldspar. The experiments were carried out using Cold Seal Pressure Vessels (CSPV) at the
165 Geology Division (University of Camerino); details on CSPV facilities, capsule preparation and
166 experimental methods are described in Arzilli and Carroll (2013).
167
168 2.2 Natural products
169 Analyzed pumice and scoria fragments are from the Lower and Upper Members of the Monte
170 Nuovo formation (Fig. 1a, b, c), respectively. Fragments and eruption levels were selected on the
171 basis of previous textural and chemical characterization (D'Oriano et al. 2005; Piochi et al. 2005;
172 Piochi et al. 2008) with the aim to analyze in major detail the textural and petrological variability in
173 products representative of the eruption phase, including new X-ray diffraction data.
174 Pumices are mostly angular clasts, yellowish in colour and with sub-spherical vesicles, from few
175 to several centimetre in dimension. Other pumices are characterized by alternating yellow and
176 brown portions and are referred to as banded pumices. Scoriae are mostly blackish clasts, generally
177 dm-sized, containing heterogeneous vesicles and often a more vesicular core and less vesicular
178 margin, with elongated vesicles in some pumice fragments. The pumice and scoria fragments
179 contain <3% of phenocrysts including mostly feldspars, subordinate magnetite and rare spinel. The

vesicularity and groundmass crystallization degree is variable (Fig. 3) (see also, D'Oriano et al. 2005; Piochi et al. 2005; Piochi et al. 2008). Microcrystallinity is determined by alkali-feldspars (anorthoclase and sanidine). It varies with vesicularity: microlites are less abundant and smaller in size in highly vesicular pumice compared with the scoria clasts. Overall, the products are denser and more crystalline upwards in the sequence, as observed by D'Oriano et al. (2005) and Piochi et al. (2005). Bands in pumice fragments are strongly parallel to each other and are associated with variations in groundmass texture: brown bands being more crystalline and less vesicular than yellowish bands (Piochi et al. 2008). The microlites have a general acicular shape with larger sizes compared with those in scoriae; some of them are curved, following the shape of adjacent vesicle, suggesting that they grew concomitantly with vesicle (Piochi et al. 2005; Piochi et al. 2008). In pumices, microlites are nearly-to-strongly aligned, and microlites and color bands share the same alignment.

Early fragmentation caused by magma-water interaction during magma ascent produced the pumices at the base of sequence (samples LM inf d and LM inf l; Fig. 1a). This is texturally (Fig. 3) testified by i) the vesicle walls that are broken and show shocking cracks, ii) their vesicularity up to 80% higher than in other pumices and scoriae; and iii) the lower groundmass crystallinity. All these associated to higher water content with respect to products higher in the sequence (Piochi et al., 2008). Textural variation of brown pumices (LMC3; Fig. 1c) and scoriae (MN4top; Fig. 1b and Fig. 3b) mostly resulted from the variable magma outgassing occurring in relation to the magma ascent dynamics (Piochi et al. 2008) during the proceeding of the eruption (D'Oriano et al. 2005; Piochi et al. 2005).

3. Analytical methods

3.1 SEM and image analysis

Electron microscope images were taken for both synthetic and natural samples in order to obtain more details on the textural features and mineralogical assemblage (Figs 3, 4, 5). Back scattered

electrons (BSE) images were collected for experimental samples using JEOL JSM-6390LA FE-SEM (at the Institute of Geochemistry and Petrology, ETH Zurich) and JEOL JSM-6500F - upgraded to 7000 series – FEG at the INGV of Rome. More details about image analysis procedure and the calculation method of crystallization kinetics are provided by Arzilli and Carroll (2013). BSE images of pumices and scoriae of Monte Nuovo were acquired through a LEO 430 SEM at "Istituto Geomare Sud – CNR" of Napoli, Italy and a ZEISS SUPRA 35 at the ''Dipartimento di Ingegneria dell'Informazione'' of the II Università di Napoli in Aversa, Italy, operating at 10 keV, and a work distance of 15 mm and 7–12 mm, respectively.

3.2 CSD analysis

The fragments from the selected natural samples were studied through CSD in order to estimate the magma residence time, knowing the relation between feldspar population density, the sizes and the specific growth rates of alkali feldspar. CSD studies provide quantitative information on relation between crystal population density and crystal length for a population of crystals. The linear relation provides estimates of time scales of magmatic processes (Marsh, 1988; Cashman and Marsh, 1988). The slope of the correlation is equal to –1/(growth rate * residence time) and the intercept is equal to the nucleation density.

Crystal dimensions and abundances of each size population were recovered through accurate image analyses by using BSE images and Adobe Photoshop ® software package. The crystals were manually segmented because the contrast between trachytic glass and feldspar microlites is weak. We were able to define the contour of each single crystal also in agglomerate structures. However, for highly crystalline samples, the geometry of each crystal was affected by some interpretation. Several elaborations were made to define different crystal geometry in agglomerates but they provided similar results. The reconstructed image was processed through ImageJ software (NIH Inage; Abramoff et al. 2004; Schneider et al. 2012) package to quantify data on crystallinity percentage and sizes. The relation between crystal population density and crystal length for a

population of crystals were finally obtained employing the CSD Corrections 1.3 program (Higgins 2000; Higgins 2002).

3.3 X-ray diffraction analysis

Selected whole-rocks and related hand-picked shards from the same sampled units used for CSD were examined by powder XRD. Samples were powered in an agate mortar and analyzed by X-ray diffraction method with the aim to further characterize mineralogy and semi-quantitative phases estimation, on larger amount of sample than that studied on thin section.

X-ray powder diffraction (XRPD) patterns were obtained by using a Panalytical X'Pert Pro diffractometer of the Istituto Nazionale di Geofisica e Vulcanologia, sezione Osservatorio Vesuviano (Naples, Italy), as illustrated in Mormone et al. (2014). Operating conditions were: CuKα radiation, 40 kV, 40 mA, 2θ range from 3 to 100°, equivalent step size 0.0179° 2θ, equivalent counting time 298.09 s per step. The X'Pert High Score Plus 2.2 d software allows qualitative and semi-quantitative data of the analysed natural powders. Semi-quantitative XRD analysis was carried out on 7 samples by using the X'Pert High Score Plus 3.0e d package interface as detailed in the Supplementary Material 1.

4. Results

4.1 Experimental samples: crystallization kinetics and textural features

The experiments performed in this study are characterized by several phases: alkali feldspar, clinopyroxene, Fe-Ti oxide, biotite, sodalite, glass and vesicles (Table 3). The sodalite (Table 3) is always generated at pressure ≤50 MPa, and it occurs at high crystal fraction of alkali feldspar (ϕ).

The experiments were texturally analyzed in order to study the crystallization kinetics of the alkali feldspar, quantifying the number density (N_a), crystallinity (ϕ), crystal size (L) and growth rates (Y_L) of alkali feldspar (Table 3). The experiments between 50 and 200 MPa show that the number density of alkali feldspar ranges from 10^4 and 10^6 cm^{-3} (Table 3) and the order of

magnitude of N_a increase with decreasing pressure. The experiments are characterized by a wide range of crystallinities of alkali feldspar (ϕ) which vary between 0.01 and 0.95. The experiments at high pressure (100, 150 and 200 MPa) and short experimental duration (7200 – 28800 s) ϕ change from 0.01 to 0.32 (Table 3). Whereas, for the same pressures but at long duration (57600 s) ϕ is ~ 0.42. The experiments at 50 MPa and $15 \leq \Delta T \leq 40$ °C, ϕ ranges between 0.29 and 0.55 Table 3. Several samples (see D69, D78, D21 and D62 in the Table 3) show that low pressure (30-50 MPa), H_2O content (1.7-2.7 wt % H_2O) and $40 \leq \Delta T \leq 115$ °C favor an extreme crystallization of alkali feldspar ($0.72 \leq \phi \leq 0.95$). Therefore, strongly intergrown textures were favored between 30 and 50 MPa, characterized by a large quantity of tiny crystals (tabular and acicular crystal intergrowth) with very low abundance of glass (Fig. 4a, b, c, i). Alkali feldspars have commonly tabular and elongated rectangular shapes (Figs 4a, b, c, i and 5b, c, d) at the different experimental conditions. Instead, spherulitic alkali feldspar crystals are more common at higher P_f ($=P_{H2O}$), and they are present in the same way both in cooling and decompression experiments. Furthermore, although the difficulty to obtain reliable chemical analysis, it was possible to establish that 1) alkali feldspars have less than 8 mol% of An and 39 to 71 mol% of Or and 2) glasses are trachytes.

The growth rates (Y_L) of alkali feldspar range from 10^{-8} to 10^{-7} cm/s (Table 3), showing a sensible decreasing at long experimental duration (57600 s), probably related to a closer approach to equilibrium at longer times.

4.2 Natural samples: textural, XRPD and CSD data

The dominant alkali-feldspar mineral phase is present in various percentages, with nearly glassy matrix (Fig. 3e) to very high abundance (Fig. 3b). X-ray diffraction patterns (see Supplementary Material 1) allow evaluating the relative proportion of anorthoclase and sanidine and the accessory minerals present in the various samples (Table 4) providing information additional to the that derived by the optical and electron microscope investigations (Fig. 3). The anorthoclase abundance is higher in the highly crystalline brown pumices (71-83%) and scoriae (55-60%). These products

284 also show small % of sodalite (~3 and ~6%, respectively). Biotite contributes to the XRPD patterns
285 of several samples with relative abundance <0.2-0.6%. Note that the biotite is absent in the scoriae
286 erupted at the end of the eruption. Furthermore, the XRPD semi-quantitative data on whole-rock
287 and related separated shards of each sample indicate comparable mineral phase percentage.
288 Therefore, the contribute of phenocrysts is not significant and the XRPD can be used to asses
289 microlite abundance, as also it results by comparing semi-quantitative data by XRPD
290 (Supplementary materials 1) and BSE images (Piochi et al., 2008).
291 Alkali feldspars are generally aligned in the bands and, sometimes, clustered in spherulitic clots.
292 No significant contortion characterizes the bands. The size and abundance of alkali feldspar
293 determined in natural samples allow us to obtain several measurements of CSDs (Fig. 6). In
294 agreement with previous analysis (D'Oriano et al. 2005; Piochi et al. 2005; Mastrolorenzo and
295 Pappalardo 2006), the size distributions of microlites appear to define two approximately linear
296 trends, a steeper one for crystals smaller than about 0.6 mm, and another, more shallow slope for
297 larger crystals; trends for different samples are nearly parallel. However, our CSDs are more
298 accurate in comparison to those in the literature that show comparable intercept values, but lower
299 crystal size as the consequence of smaller area investigated by previous authors (Piochi et al.,
300 2005). The stratigraphically lower pumices show a simple CSD with a unique growth trend, while
301 scoriae are characterized by two trends that show two timing of crystal growth (Fig. 6). Therefore,
302 the smaller microlites define CSD curves with slopes that range from -22 to -8 and an intercept at
303 10^{-11} mm^{-2}; instead the curves for larger microlites have slopes between -2 and -7 and extrapolated
304 intercepts at 10^{-9}-10^{-11} mm^{-2} (Table 5). Lower slope values are generally determined in the lower
305 vesicular brownish bands and black scoria (c2s 9-12 – 1 and MN4 top 06 – 1, respectively, in Table
306 5); whereas higher slopes are from the highly vesicular yellow glass.
307
308 5. Discussion
309 5.1 The rapid change of crystallinity: the role of P_{H2O} and ΔT

310 The cooling experiments performed by Arzilli and Carroll (2013) show that ϕ varies between
311 0.05 and 0.64, instead, here we show that ϕ could be ranged from 0.01 to 0.93 a certain conditions.
312 This can be also observed in decompression experiments: ϕ shows similar variation, from 0.13 to
313 0.76 for "decompression + cooling" experiments and from 0.09 and 0.77 for isothermal
314 decompression (Arzilli and Carroll 2013). Here we show that in the latter kind of experiment ϕ
315 reaches 0.95 at 30 MPa and long duration (14 h). Instead, the abundances of clinopyroxene and
316 magnetite remain low (0.01 to 0.10) for this feldspar-dominated bulk composition (Arzilli and
317 Carroll, 2013).
318 The abundance and morphologies of alkali feldspar are linked to P_f (= P_{H2O}), water content, ΔT
319 and experimental duration (as observed by Arzilli and Carroll, 2013). By combining our results with
320 those of Arzilli and Carroll (2013) we show that cooling experiments at 50 and 70 MPa can produce
321 higher ϕ than those at 100, 150 and 200 MPa (Fig. 7a, b). The relation between N_a and ΔT as a
322 function of P_f for cooling experiments (Fig. 7c) show that at 70 and 100 MPa, N_a increases as ΔT
323 increases, whereas for experiments at 50 MPa, N_a is almost constant with ΔT. The main evidence is
324 that at low ΔT, N_a increases as P_f decreases and the nucleation process is favored at low pressure,
325 with lower melt water contents. The diagram in Fig. 7d shows also that N_a is almost constant with
326 the time, confirming that P_f (=P_{H2O}) and ΔT play a crucial role on the nucleation of alkali feldspar,
327 producing either high or low crystallized rocks over the limited temperature range investigated.
328 The decompression experiments show the same relations observed for cooling experiments. The
329 high crystallinity textures are produced at 30 and 50 MPa (Fig. 8a, b). The order of magnitude of N_a
330 for experiments at 30 and 50 MPa is up to three times higher than experiments at 70, 100 and 150
331 MPa (Fig. 8c), increasing with decreasing water content. The exceptions are the samples at 50 MPa
332 (ΔT = 25 °C) and that at 70 MPa (ΔT = 14 °C), which have a low value of N_a similar to the
333 experiments at 150 MPa (Fig. 8c). Probably, small ΔT could slow down the nucleation process,
334 favoring the growth. As shown above from cooling experiments, the orders of magnitude of N_a is

almost constant over time, while low pressures facilitate greater nucleation of alkali feldspar (Fig. 8c,d). The latter diagram highlights also that similar ΔT (~40 °C) can produce different orders of magnitude of N_a, confirming that a strong nucleation of alkali feldspar is induced at low pressure.

Although we have studied the isobaric cooling and isothermal decompression processes, we have not distinguished the concept of undercooling (ΔT) and effective undercooling (ΔT_{eff}), the effective undercooling related to decompression process at constant temperature (Hammer and Rutherford, 2002) because, as shown by Arzilli and Carroll (2013), under the same experimental conditions, both processes produce similar crystallization kinetics. Furthermore, we performed "cooling + decompression" experiments where it is difficult to separate ΔT and ΔT_{eff}. The comparison between cooling and decompression experiments shows that at similar conditions, in terms of P_f, ΔT and superheating, cooling and decompression experiments produce similar N_a and ϕ. This may mean that the distinction between ΔT (related to cooling process) and ΔT_{eff} is useless when a single fast step of cooling and decompression occurs.

The nucleation of large amount of crystals (tabular and acicular crystal intergrowth) was favored at low pressure (Figs 4, 7 and 8) and not necessarily at low ΔT, instead it was reduced at high pressure (Figs 5, 7 and 8), highlighting that a small decrease in pressure can induce a dramatic increase of crystallinity.

5.2 Experimental vs natural materials

The experiments produced material texturally comparable with natural products, although the pyroxene occurrence represents the most important discrepancy. This may depend on the starting experimental conditions as pyroxenes are already contained in ZAC, and the oxygen fugacity of the CSPV (~NNO+1 log units) may also be different in comparison to that of the Monte Nuovo system.

The alkali feldspar morphologies of natural samples (Fig. 3) are similar to in the experimental ones (Figs 4 and 5). Experimental alkali feldspars are characterized by elongated rectangular crystals and they occur in clots (Fig. 4) or isolated in the glass (Fig. 5), as in the natural pumices.

361 Both types of decompression experiments at 50 MPa produced similar textures to natural scoriae,
362 with high crystallinity and aligned tabular or elongated rectangular crystals (see Figs 3b and 5c),
363 also including magnetite and sodalite crystals (Table 4). These highly crystalline charges also show
364 vesicles with irregular margin similarly to the natural scoriae. Furthermore, the Or content of the
365 synthetic alkali feldspars and those of natural ones are similar (D'Oriano et al. 2005; Piochi et al.
366 2005; Piochi et al. 2008).
367 Diagrams in Fig. 9a and b allow quantitatively comparing experimental and natural crystalline
368 textures. Fig. 9a shows a relation between N_a and ϕ obtained through cooling experiments, where ϕ
369 increases as growth dominates the crystallization process. Instead, N_a increases as nucleation
370 dominates the process. In particular, N_a increases as P_f (therefore water content) decreases (Fig.
371 9a), showing that P_{H2O} and the water content have an important effect on textural evolution. Low
372 experimental pressure and low water content seems to enhance nucleation density, thus producing
373 more alkali feldspar nuclei. The diagram also suggests that natural alkali feldspars of the glassy
374 pumices must crystallize at ≥70 MPa, based on comparison of relative nucleation densities.
375 Sodalite absence and biotite occurrence in these samples support such barometric conditions. In
376 agreement with Mastrolorenzo and Pappalardo (2006), glassy pumices are characterized by low N_a
377 of alkali feldspar. Moreover, ϕ of natural alkali feldspars is between 0.01 and 0.30, suggesting a
378 crystallization event at low ΔT, therefore crystallization temperature could be close to the liquidus
379 of alkali feldspar. Instead, data from more crystal-rich pumice and scoria resemble most closely
380 experimental samples produced at 70 MPa pressure, under less than 69 °C and 39 °C of ΔT (Arzilli
381 and Carroll, 2013), respectively. Nevertheless, these experiments do not reproduce sodalite.
382 Notably, the natural sample with ϕ ~0.95 (Fig. 9a; D'Oriano et al. 2005) could be reproduced at
383 high ΔT (>60 °C), in agreement with the experiments performed in this study (D69, D78 and D62).
384 The holocrystalline texture probably requires low pressures (between 50 and 30 MPa) and more
385 time for crystal growth, supporting a possible origin involving magma stagnation in the conduit (in
386 agreement with D'Oriano et al. 2005). Hence, the sodalite occurrence should be due to the high

crystallinity and the enrichment of Cl in the residual melt (Carroll 2005).

The results of "decompression + cooling" and isothermal decompression experiments are shown separately in Table 3, but for the discussion they are included together to have a wider range of potential pre- and syn-eruptive conditions. Decompression experiments are characterized by two populations of samples which have differences in nucleation density (Fig. 9b). The first population at low pressure (30 MPa < P_f < 50 MPa) has values of N_a between 10^6 and 10^7 cm^{-2}, exceeding values observed in the natural samples. In contrast, the second group off higher P experiments (100 MPa < P_f < 150 MPa), has values of N_a between 10^4 and 10^5 cm^{-2}, and closely resemble observations on natural scoria and pumices. The experiments at 50 MPa (charge D81), 70 MPa (charge D82), 100 MPa (charge D80) and 150 MPa (charge D55) are characterized by N_a = ~10^5 cm^{-2} and ϕ between ~0.10 and ~0.30 (see Table 3 and the results of Arzilli and Carroll, 2013), therefore comparable with poorly crystallized natural pumice. As a whole, the ϕ of alkali feldspar = 0.01-0.30 in the pumice fragments implies ΔT<50 °C, the increase up to 0.40-0.60 in the scoriae, as well as the highest one at 0.95 (D'Oriano et al. 2005), requires higher ΔT and low pressure. In particular, scoriae trend toward experiments at ≤70 MPa in terms of N_a and ϕ, as well as containing traces of sodalite.

Experimental results suggest that crystallization of natural alkali feldspar occurred: i) between 200 and 70 MPa and, mostly 150-100 MPa (low ΔT), at temperature between 750 °C and 825 °C, in water saturated cooling conditions or/and ii) at >50, and mostly 150 MPa, at temperature between 750 and 840 °C, if melt decompressed. Furthermore, the absence or presence of sodalite crystals indicate that natural glassy samples register P ≥50 MPa, whereas lower pressure corresponds to the more crystalline brown pumices and scoriae. Thus, we constrain: the crystallization in the brown pumice and scoriae occurred over a longer time compared with pumice sample crystallization. Furthermore, for water saturated conditions and in the 200-50 MPa pressure range, temperature ≥850 °C means that conditions are always above the alkali feldspar liquidus. Therefore, natural

412 alkali feldspar crystallization between 200 and 150 MPa needs temperature of 750-775 °C, or 800-
413 825 °C at 100 to 70 MPa, or 840-860 °C at 50 MPa.
414
415 5.3 Magma residence time deduced from growth rates and CSDs
416 Measurements of Crystal Size Distribution (CSD), when combined with experimental growth
417 rate data for alkali feldspar (Y_L), can help us to better constrain the time of magma crystallization
418 just before fragmentation (e.g., Marsh 1988; Cashman and Marsh 1988; Higgins 1996; Armienti et
419 al. 2007). Following Piochi et al. (2005) and D'Oriano et al. (2005), these times may correspond to
420 the time of magma crystallization in the chamber (cooling-dominated conditions) or to magma
421 movements in the volcanic conduit (decompression-dominated conditions).
422 We use new data on both CSDs (Fig. 6) and feldspar growth rate in recalculating crystallization
423 times (t_r) for the Monte Nuovo magma. The estimated growth rate (Y_L) mostly varies between
424 $1.1*10^{-8}$ and $7.2*10^{-7}$ cm/s (considering Y_L obtained in this study and from Arzilli and Carroll,
425 2013), with an isolated higher value at $1.2*10^{-6}$ cm/s and the mean Y_L equal to $2.21*10^{-7}$ cm/s
426 (Table 5). Because the crystal growth rate varies by up to two orders of magnitude, significant
427 variations of the magma timing must be expected. Therefore, the crystallization time is from few
428 months to few hours. However, the mean Y_L suggests that magma was stored for a few days in the
429 subsurface and the ascent lasted a few hours. Notably, the lower CSD slopes, i.e., the higher
430 residence times, characterize the most crystalline matrices. This is in agreement with the feldspar
431 chemistry detected by XRPD and reproduced in longer experiments (Supplementary Material 1).
432
433 5.4 Implication for magma dynamics
434 Experimental results suggest that the crystallization of alkali feldspars in magma erupted during
435 the Monte Nuovo eruption started between <200 and 100 MPa when temperature was close to the
436 liquidus of alkali feldspar (at least 825 °C). This is also supported by the few biotite in our natural
437 products (Supplementary Materials 1); in fact, previous experimental work and the present results

438 (see charges D20, D15, D17, D25 in Tables 1 and 2) on trachytic melts indicate the stability field of
439 biotite at pressure >135 MPa (Fabbrizio and Carroll 2008). Based on these results, we constrain the
440 pre-eruptive magma storage at a depth allowing the biotite crystallization, i.e., >4 km, comparable
441 or slightly higher than hypothesized in Piochi et al. (2005). Furthermore, our experimental data
442 indicate that the early erupted Monte Nuovo magma (LM unit) fragmented before reaching 50-70
443 MPa (~2 km of depth). Pre-eruptive pressure estimates (50-70 MPa) suggested by our results are in
444 agreement with the pre-eruptive fH_2O of phlegraean magma at ~70 MPa estimated by Fabbrizio et
445 al. (2009), implying a repetitive behaviour for the volcanic system. Low ΔT can be suggested for
446 the early erupted products, in agreement with previous inferences (D'Oriano et al., 2005). Our
447 results indicate lower pressures for the later erupted magma (i.e., scoriae in the Upper Member)
448 registers. The high groundmass crystallinity with alkali feldspar as prevalent phase and the sodalite
449 occurrence in these later erupted fragments (Table 4) suggest effective undercoolings of several
450 hundreds °C (Fig. 9) and pressure of crystallization below 50 MPa. Notably, Mastrolorenzo and
451 Pappalardo (2006) also placed the fragmentation level of phlegraean volcanoes between 10 and 30
452 MPa, but without distinction among eruptive phases. Decompression was the main process
453 controlling the textures of the Monte Nuovo products, in agreement with occurrence of microlites
454 that are curved following the morphology of adjacent vesicles, suggesting that they grew
455 concomitantly with vesicles (Piochi et al., 2005; Piochi et al. 2008). In particular, our results
456 support the idea that open-system degassing promoted massive crystallization in later erupted
457 magma (Fig. 3), moving the melt towards the most evolved compositions observed (D'Oriano et al.,
458 2005; Piochi et al., 2008).
459 The magma ascent from the storage (≤135 MPa) to fragmentation (≤50 MPa) pressures occurred
460 rapidly, with timescales on the order of hours suggested by our CSD results (see Table 5). Fabbrizio
461 and Carroll (2008) also suggested that the travel of the biotite-bearing phlegraean magma from
462 reservoir at depth of c. 7 km (~200 MPa) to the surface was rapid, based on dissolution rate data of
463 biotites (hours to a maximum of 1-2 days; Fabbrizio and Carroll, 2008). Low ascent rate results in

464 dissolution of biotite. Therefore, the magma ascent rate is estimated in 400-100 m/h from a depth
465 of 4-5 km (biotite-stable). Magma storage of some days in the shallow crust is indicated by the
466 occurrence of some phenocrysts (that forms slope >-10, Table 5, Fig. 6), whereas the smaller-sized
467 crystals (and the CSD with higher slopes; Table 5 and Fig. 6) were able to crystallize in few hours.
468 These results better constrain previous reconstruction of this eruption (Piochi et al. 2005; D'Oriano
469 et al. 2005). The detected CSD variation reflects the textural features of samples, resulting from
470 small differences in rates of magma ascent, crystallization, and degassing (see also D'Oriano et al.
471 2005; Piochi et al. 2005, 2008) during eruption. The LM vesicular pumices (early erupted; Fig. 1)
472 register the magmatic fragmentation generated by magma-water interaction following gas
473 expansion; while syn-eruptive outgassing-induced crystallization produced brown pumices and
474 scoriae (later erupted magma; Fig. 1) in the course of the eruption. The most crystalline and less
475 vesicular scoriae contain lower amount of H_2O than LM microlite-poor and vesicle-rich pumices
476 (Piochi et al. 2008).
477 The Phlegraean trachyte can rapidly crystallize large crystal fractions of alkali feldspar, over
478 small pressure-temperature intervals, as shown in this experimental study, and this can strongly
479 modify the rheology of a trachytic magma, favoring rapid changes in eruptive style, if not the
480 ending of the eruption. The obtained results allow us to constrain the magma processes producing
481 the change in the eruptive style from pumice to scoria type deposits, due to an increase of magma
482 viscosity (Caricchi et al., 2008; Vona et al. 2013), quantitatively supporting the idea of D'Oriano et
483 al. (2005) about the plug generation in the volcanic conduit in the last eruptive phase. In fact,
484 values of ϕ between 0.80 and 0.90 observed in the natural scoriae of Monte Nuovo produced in this
485 phase requires higher ΔT and lower P, as suggested from the experiments. Therefore, the same
486 experimental data indicates lowering water content, corroborating hypothesis of open degassing
487 conditions during the scoria eruption (D'Oriano et al. 2005; Piochi et al. 2008). The abundance of
488 crystals in the scoria deposits reaching values higher than 90% (D'Oriano et al. 2005) may be
489 related to high ΔT and low P_f ($=P_{H2O}$) or long residence of the magma in shallower part ($P_f < 50$

MPa) of the conduit, as shown from our results (see samples D69, D78 and D62). ΔT can enhance crystal fraction by increasing crystal nucleation rate, changing the magma rheology toward more viscous behaviour as crystal content increases. This is in agreement with evidence showing that in a closed magmatic system undergoing continuous decompression and cooling, crystal could only become larger and more numerous with time (Wolf and Eichelberger 1997). Futhermore, Melnik (2000) shows that the high viscosity value of the magma in the conduit is probably responsible for increasing pressurization, and our results justify a potential overpressure in the conduit, which may have triggered the final vulcanian explosion of Monte Nuovo.

Finally, the coexistence of pumices with different vesicle and microlite textures (for example, samples LM inf l, LM in d and LM c3) suggests a complex process of magma ascent dynamics. Mingling between magmas that reached the surface through different pathways and pressure-temperature-time conditions in the subsurface or, following D'Oriano et al. (2005), the horizontal zoning of magma conditions in the conduit are possibilities to be further investigated.

6. Conclusion

The comparison between experimental data and data from natural samples furnishes a set of P-T-H_2O content conditions for trachytic magmas valid for the Monte Nuovo eruption, at the Campi Flegrei. The cooling and decompression experiments allowed reproducing textures observed in pumices and scoriae produced during the 1538 AD eruption. First, the obtained results indicate that the juvenile pyroclastic components i) represent the magma at or near the fragmentation surface and ii) register the magma condition within the volcanic conduit. Also, this eruption requires a water-saturated magma stored at around 135 MPa, near the liquidus temperature of alkali feldspar; its ascent toward the surface lasted a few hours to several days. Months of magma crystallization are registered in some pyroclastic fragments. Therefore, the intense seismicity, gas emissions and ground deformations described by the historical chronicles (see Guidoboni and Ciucciarelli 2011 and references therein) in the months before the eruption are phenomena related to the volcanic

unrest. Our results, instead, suggest that the low seismicity and gas emissions that affected the Campi Flegrei area prior to at least 1530-1536 AD are not directly connected to the unrest and should be related either to the deeper magmatic system or to the hydrothermal environment. Our results do not furnish direct information concerning what triggered the eruption at Monte Nuovo.

As a whole, this experimental study offers a set of pressure, temperature and undercooling (water saturated) conditions, useful to constrain the timescale and to better understand the magma behavior of numerous phlegraean eruptions, starting from the texture of their eruptive products. In fact, alkali feldspar is the main crystal phase in the phlegraean rocks and, as shown for the Monte Nuovo eruption, its crystallization could be started between 7 and 4 km depth (≤200 MPa) and proceed in the conduit, where the magma ascent was faster and texture was effectually frozen in, located mostly between 2 and 3 km (50-70 MPa). The sodalite absence in most of the natural samples impies that magmas generally fragmented before reaching 30-50 MPa (pressure for sodalite stability) or magmas stored at these levels only occasionally were erupted. Furthermore, the temperature of the magma, in pre-eruptive conditions, is most likely between 825 and 840 °C (close to the liquidus of alkali feldspar). Notably, this study allows us to tentatively forecast the pre-eruptive magma conditions and timescales of future events in the Campi Flegrei area.

Acknowledgements

This work was supported by the 2005–2006 INGV-DPC project V3-2/UR14 (M. Piochi) and PRIN 2009 (R. Moretti), FAR 2012 (M. R. Carroll). The authors are indebted to N. Cennamo (II University of Napoli, Napoli, Italy) for help with the BSE image acquisition and Luigi Zeni (II University of Napoli, Napoli, Italy) that allowed access to the laboratory. The VULCAMED project provided funds to install in October 2012 the XRD laboratory at the Istituto Nazionale di Geofisica e Vulcanologia, in Naples. We would like to thank P. Scarlato, C. Freda and A. Cavallo for assistance with the SEM at INGV, Rome. We thank also Prof. M. W. Schmidt for providing

SEM access at ETH of Zurich (Institute of Geochemistry and Petrology). We also thank P. Landi for SEM analysis and M. R. Cicconi for assistance during experiments.

References

Abramoff MD, Magalhaes PJ, Ram SJ (2004) Image Processing with ImageJ. Biophotonics International 11:36-42

Armienti P, Francalanci L, Landi P (2007) Textural effects of steady state behaviour of the Stromboli feeding system. J Volcanol Geoth Res 160:86-98

Arzilli F, Carroll MR (2013) Crystallization kinetics of alkali feldspars in cooling and decompression-induced crystallization experiments in trachytic melt. Contrib Mineral Petrol 166:1011–1027

Boivin P, Bourdier JL, Camus G, de Goer de Herve A, Gourgaud A, Kieffer G, Mergoil JM, Vincent PM, Auby R (1982) Influence de la Nature des Magmas sur l'Activité Phreatomagmatique: Approche Volcanologique et Thermodynamique. Bull Volcanol 45:25-39

Calzolaio M, Arzilli F, Carroll MR (2010) Growth rate of alkali feldspars in decompression-induced crystallization experiments in a trachytic melt of the Phlegraean Fields (Napoli, Italy). Eur J Mineral 22:485-493

Caricchi L, Giordano G, Burlini L, Ulmer P, Romano C (2008) Rheological properties of magma from the 1538 eruption of Monte Nuovo (Phlegrean Fields, Italy): An experimental study. Chemical Geology 256: 158-171

Carroll MR (2005) Chlorine solubility in evolved alkaline magmas. An Geophys 48: 619-631

Cashman KV, Marsh BD (1988) Crystal size distribution (CSD) in rocks and the kinetics and dynamics of crystallization II: Makaopuhi lava lake. Contrib Mineral Petrol 99:292–305

Couch S, Sparks RSJ, Carroll MR (2003) The kinetics of degassing- induced crystallization at Soufriere Hills volcano, Montserrat. J Petrol 44:1477–1502

567 Del Gaudio C, Aquino I, Ricciardi G.P, Ricco C, Scandone R (2010) Unrest episodes at Campi
568 Flegrei: A reconstruction of vertical ground movements during 1905–2009. J Volcanol
569 Geotherm Res 195:48–56
570 Di Girolamo P, Ghiara MR, Lirer L, Munno R, Rolandi G, Stanzione D (1984) Volcanology and
571 petrology of Campi Flegrei. Boll Soc Geol It 103:349-413
572 Di Matteo V, Carroll MR, Behrens H, Vetere F, Brooker R (2004) Water solubility in trachytic
573 melts. Chem Geol 213:187-196
574 Di Renzo V, Arienzo I, Civetta L, D'Antonio M, Tonarini S, Vito MD, Orsi G (2011) The
575 magmatic feeding system of the Campi Flegrei caldera: Architecture and temporal evolution.
576 Chem Geol 281:227-241
577 Di Vito M, Lirer L, Mastrolorenzo G, Rolandi G (1987) The 1538 Monte Nuovo eruption (Campi
578 Flegrei, Italy). Bull Volcanol 49:608-615
579 Di Vito MA, Isaia R, Orsi G, Southon J, de Vita S, D'Antonio M, Pappalardo L, Piochi M (1999)
580 Volcanism and deformation since 12,000 years at the Campi Flegrei caldera (Italy). J Volcanol
581 Geoth Res 91:221-246
582 D'Oriano C, Poggianti E, Bertagnini A, Cioni R, Landi P, Polacci M, Rosi M (2005) Changes in
583 eruptive style during the A.D. 1538 Monte Nuovo eruption (Phlegrean Fields, Italy): the role of
584 syn-eruptive crystallization. Bull Volcanol 67:601-621
585 Dowty E (1980) Crystal growth and nucleation theory and the numerical simulation of igneous
586 crystallization. In: Hargraves RB (ed) The physics of magmatic processes. Princeton University
587 Press, Princeton, NJ, pp 419–485
588 Fabbrizio A, Carroll MR (2008) Experimental constraints on the differentiation process and pre-
589 eruptive conditions in the magmatic system of Phlegraean Fields (Naples, Italy). J Volcanol
590 Geoth Res 171:88-102
591 Fabbrizio A, Scaillet B, Carroll MR (2009) Estimation of pre-eruptive magmatic water fugacity in
592 the Phlegrean Fields, Naples, Italy. Eur J Mineral 21:107–116

593 Fedele L, Scarpati C, Lanphere M, Melluso L, Morra V, Perrotta A, Ricci G (2008) The Breccia
594 Museo formation, Campi Flegrei, southern Italy: geochronology, chemostratigraphy and
595 relationship with the Campanian Ignimbrite eruption. Bull Volcanol 70:1189-1219
596 Fedele L, Insinga D, Calvert A, Morra V, Perrotta A, Scarpati C (2012) Reply to the comment on
597 the article 40Ar/39Ar dating of tuff vents in the Campi Flegrei caldera (southern Italy): toward a
598 new chronostratigraphic reconstruction of the Holocene volcanic activity by Isaia et al. Bull
599 Volcanol 74:1-3
600 Geschwind C, Rutherford MJ (1995) Crystallization of microlites during magma ascent: the fluid
601 mechanics of 1980-1986 eruptions at Mount St Helens. Bull Volcanol 57:356–370
602 Guidoboni E, Ciuccarelli C (2011) The Campi Flegrei caldera: historical revision and new data on
603 seismic crises, bradyseisms, the Monte Nuovo eruption and ensuing earthquakes (twelfth century
604 1582 AD). Bull Volcanol 73:655–677
605 Hammer JE, Rutherford MJ (2002) An experimental study of the kinetics of decompression-
606 induced crystallization in silicic melt. J Geophys Res 107:2021
607 Higgins MD (1996) Magma dynamics beneath Kameni volcano, Thera Greece, as revealed by
608 crystal size and shape measurements. J Volcanol Geoth Res 70:37-48
609 Higgins MD (2000) Measurements of crystal size distributions. Am Mineral 85:1105–1116
610 Higgins MD (2002) Closure in crystal size distributions (CSD), verification of CSD calculations,
611 and the significance of CSD fans. Am Mineral 87:171–175
612 Kirkpatrik RJ (1975) Crystal growth from a melt: a review. Am Mineral 60:798–814
613 Isaia R, Marianelli P, Sbrana A (2009) Caldera unrest prior to intense volcanism in Campi Flegrei
614 (Italy) at 4.0 ka B.P.: Implications for caldera dynamics and future eruptive scenarios. Geophys
615 Res Lett 36: L21303
616 Le Bas MJ, Le Maitre RW, Streckeisen A, Zanettin B (1986) A chemical classification of volcanic
617 rocks based on the total alkali-silica diagram. J Petrol 27: 745-750
618 Lirer L, Luongo G, Scandone R. (1987). On the volcanological evolution of Campi Flegrei. Eos

Trans AGU 68:226

Marsh BD (1988) Crystal size distribution (CSD) in rocks and the kinetics and dynamics of crystallization. Contrib Mineral Petrol 99:277–291

Marsh BD, (1998) On the interpretation of crystal size distributions in magmatic systems. J Petrol 39:553–599

Martel C (2012) Eruption dynamics inferred from microlite crystallization experiments: Application to Plinian and dome-forming eruptions of Mt Pelée e (Martinique, Lesser Antilles). J Petrol 53:699-725

Mastrolorenzo G, Pappalardo L (2006) Magma degassing and crystallization processes during eruptions of high-risk Neapolitan-volcanoes: Evidence of common equilibrium rising processes in alkaline magmas. Earth Planet Sci Lett 250:164–181

Melnik O (2000) Dynamics of two-phase conduit flow of high-viscosity gas- saturated magma: large variations of sustained explosive eruption intensity. Bull Volcanol 62:153–170

Melluso L , Morra V, Annamaria Perrotta A, Scarpati C, Adabbo M (1995) The eruption of The Breccia Museo (Campi Flegrei, Italy) : Fractional crystallization processes in a shallow, zoned magma chamber and implications for the eruptive dynamics. J Volc Geophys Res 68:325-339

Mormone A, Piochi M, Bellatreccia F, De Astis G, Moretti R, Ventura GD, Cavallo A, Mangiacapra A (2011) A CO_2-rich magma source beneath the Phlegraean Volcanic District (Southern Italy): Evidence from a melt inclusion study. Chem Geol 287:66–80

Mormone A, Piochi M, Troise C, De Natale G (2014). Il laboratorio di Diffrattometria a raggi X dell'Osservatorio Vesuviano (Istituto Nazionale di Geofisica e Vulcanologia, Napoli): identificazione e stima quantitativa delle fasi in campioni polverizzati. Rapporti tecnici INGV, 279: 7-21, ISSN 2039-7941

Parascandola A (1947) I fenomeni bradisismici del Serapeo di Pozzuoli. Genovese, Napoli

Piochi M, Mastrolorenzo G, Pappalardo L (2005) Magma ascent and eruptive processes from textural and compositional features of Monte Nuovo pyroclastic products, Campi Flegrei, Italy.

645 Bull Volcanol 67:663– 678
646 Piochi M, Polacci M, De Astis G, Zanetti A, Mangiacapra A, Vannucci R, Giordano D (2008)
647 Texture and composition of pumices and scoriae from the Campi Flegrei caldera (Italy):
648 Implications on the dynamics of explosive eruptions. Geochem Geophys Geosyst 9:Q03013
649 Rosi M, Sbrana A, Principe C (1983) The Phlegrean Fields: structural evolution, volcanic history
650 and eruptive mechanism. J Volcanol Geotherm Res 17:273-288
651 Rosi M, Sbrana A (1987) The Phlegrean Fields. CNR Quaderni di La Ricerca Scientifica di La
652 Ricerca Scientifica
653 Schneider CA, Rasband WS, Eliceiri KW (2012) NIH Image to ImageJ: 25 years of image analysis.
654 Nature Methods 9:671-675
655 Smith VC, Isaia R, Pearce N (2011) Tephrostratigraphy and glass compositions of post-15 kyr
656 Campi Flegrei eruptions: implications for eruption history and chronostratigraphic markers. Quat
657 Scie Rev 30: 3638-3660
658 Swanson SE (1977) Relation of nucleation and crystal-growth rate to the development of granitic
659 textures. Am Mineral 62:966–978
660 Vona A and Romano C (2013) The effects of undercooling and deformation rates on the
661 crystallization kinetics of Stromboli and Etna basalts. Contrib Mineral Petrol 166(2):491-509
662 Wolf KJ, Eichelberger JC (1997) Syneruptive mixing, degassing, and crystallization at Redoubt
663 Volcano, eruption of Decem- ber 1989 to May 1990. J Volcanol Geoth Res 75:19–37
664

Figure captions

Figure 1: The Monte Nuovo tuff cone location (a) with image of the lowermost ash- to sand-levels and the uppermost scoria deposits (b and c, respectively). The diagrams show the timing of the phenomena preceding the eruption since 1470 AD (d) and 1538 (e), on the basis of Guidoboni and Ciucciarelli (2011). The d and e diagrams indicate the time of occurrence for seismicity (vertical bars), flow output (cloud) and ground deformation (arrows and dotted lines, right concavity meaning inflation and viceversa). The relation between phenomena and outcrops is also indicated. The onset for microlite growth as suggested by CSD is also indicated. The brown pumice and scoria samples location is indicated by black boxes in panels a and b. The sampling site of the early erupted yellow pumices of LM inf d and LM inf l is in panel a.

Figure 2: TAS (Le Bas et al. 1986), on the left, and Alkali vs. CaO, on the right, diagrams for the Monte Nuovo natural glasses and ZAC bulk rock. Data on natural glass and whole-rocks from Piochi et al. (2008), Rosi and Sbrana (1987), D'Oriano et al. (2005).

Figure 3: I have changed contrast-maybe better to see phases Groundmass texture of natural pumice (samples: c1 1-7, c2s 9-12, infl 8-12, infsc 02-05) and scoriae (samples: MN3/1, MN4top) from base upwards in the stratigraphic sequence. Samples MN3/1 (a) and MN4top (b) are two scorias upwards in the sequence. Note the cuspate shape of vesicle and the magnetite occurrence in the most crystallized and low-vesicular MN4top. Samples c1 1-7 (c) and c2s 9-12 (d) evidence the groundmass crystallinity and vesicularity feature of a yellowish and a brown pumice, respectively, within the main pyroclastic unit. Note the microlite alignment and the curved shape of several crystals. Rare microlites and high vesiculation of pumice at the base of the flow sequence. In particular, sample infl 8-12 (e) shows the cracks (white arrows) produced by water/magma interaction. Sample infsc 02-05 (f) is a banded pumice within the main pyroclastic unit

characterized by low crystal abundance and higher vesiculation of yellowish band (on the left) with respect of the adjacent brown sector. White bars are 100 μm.

Figure 4: Backscattered SEM images of textures obtained at low pressure (50 and 30 MPa) from isobaric cooling, "decompression+ cooling" and isothermal decompression experiments. Cooling experiments: (a) D33 (P_f =50 MPa, ΔT = 25 °C); (b) D10 (P_f =50 MPa, ΔT = 40 °C); (c) D69 (P_f =50 MPa, ΔT = 115 °C). "Decompression+ cooling" experiments: (d) D45 (P_f =50 MPa, ΔT = 115 °C); (e) D43 (P_f =50 MPa, ΔT = 115 °C); (f) D47 (P_f =30 MPa, ΔT = 140 °C). Isothermal decompression experiments: (g) D57 (P_f =50 MPa, ΔT = 40 °C); (h) D60 (P_f =30 MPa, ; ΔT = 65 °C); (i) D62 (P_f =30 MPa, ΔT = 65 °C). The samples D33, D10, D69 and D62 were performed in this study, the other ones are data of Arzilli and Carroll (2013).

Figure 5: Backscattered SEM images of textures obtained at high pressure (200, 150, 100 and 70 MPa) from isobaric cooling, "decompression+ cooling" and isothermal decompression experiments. Cooling experiments: (a) D1 (P_f =200 MPa, ΔT = 20 °C); (b) D15 (P_f =150 MPa, ΔT = 17 °C); (c) D6 (P_f =100 MPa, ΔT = 19 °C). "Decompression+ cooling" experiments: (d) D17 (P_f =150 MPa, ΔT = 17 °C); (e) D55 (P_f =150 MPa, ΔT = 42 °C); (f) D51 (P_f =100 MPa, ΔT = 69 °C). Isothermal decompression experiments: (g) D80 (P_f =100 MPa, ΔT = 19 °C); (h) D82 (P_f =70 MPa, ; ΔT = 14 °C); (i) D82 (P_f =70 MPa, ΔT = 14 °C). The samples D15, D6 and D17 were performed in this study, the other ones are data of Arzilli and Carroll (2013).

Figure 6: CSDs of early erupted low-crystalline and highly vesicular pumice (left), brown pumices intermediate in the stratigraphic sequence (central diagram) and scoriae (right diagram). Note the occurrence of two microlites population and the similarity of slopes of smaller microlites.

716 Figure 7: The relation of ϕ and N_a with P_f, ΔT and t_{exp} in cooling experiments. (a) Relation
717 between crystal fraction of alkali feldspar (ϕ) and ΔT as a function of P_f. (b) Relation between
718 crystal fraction of alkali feldspar (ϕ) and t_{exp} as a function of P_f and ΔT. (c) Relation between N_a and
719 ΔT as a function of P_f. (d) Relation between N_a and t_{exp} as a function of P_f and ΔT.
720
721 Figure 8: The relation of ϕ and N_a with P_f, ΔT and t_{exp} in "decompressio+cooling" and isothermal
722 decompression experiments. (a) Relation between crystal fraction of alkali feldspar (ϕ) and ΔT as a
723 function of P_f. (b) Relation between crystal fraction of alkali feldspar (ϕ) and t_{exp} as a function of P_f
724 and ΔT. (c) Relation between N_a and ΔT as a function of P_f. (d) Relation between N_a and t_{exp} as a
725 function of P_f and ΔT.
726
727 Figure 9: N_a vs ϕ. a) Relation between N_a (nucleation density) and ϕ (crystallinity) as a function
728 of P_f and ΔT for cooling experiments and natural samples of Monte Nuovo (pumices and scoriae);
729 b) relation between N_a and ϕ as a function of P_f and ΔT for both types of decompression
730 experiments and natural samples of Monte Nuovo (pumices and scoriae).

Figure 1

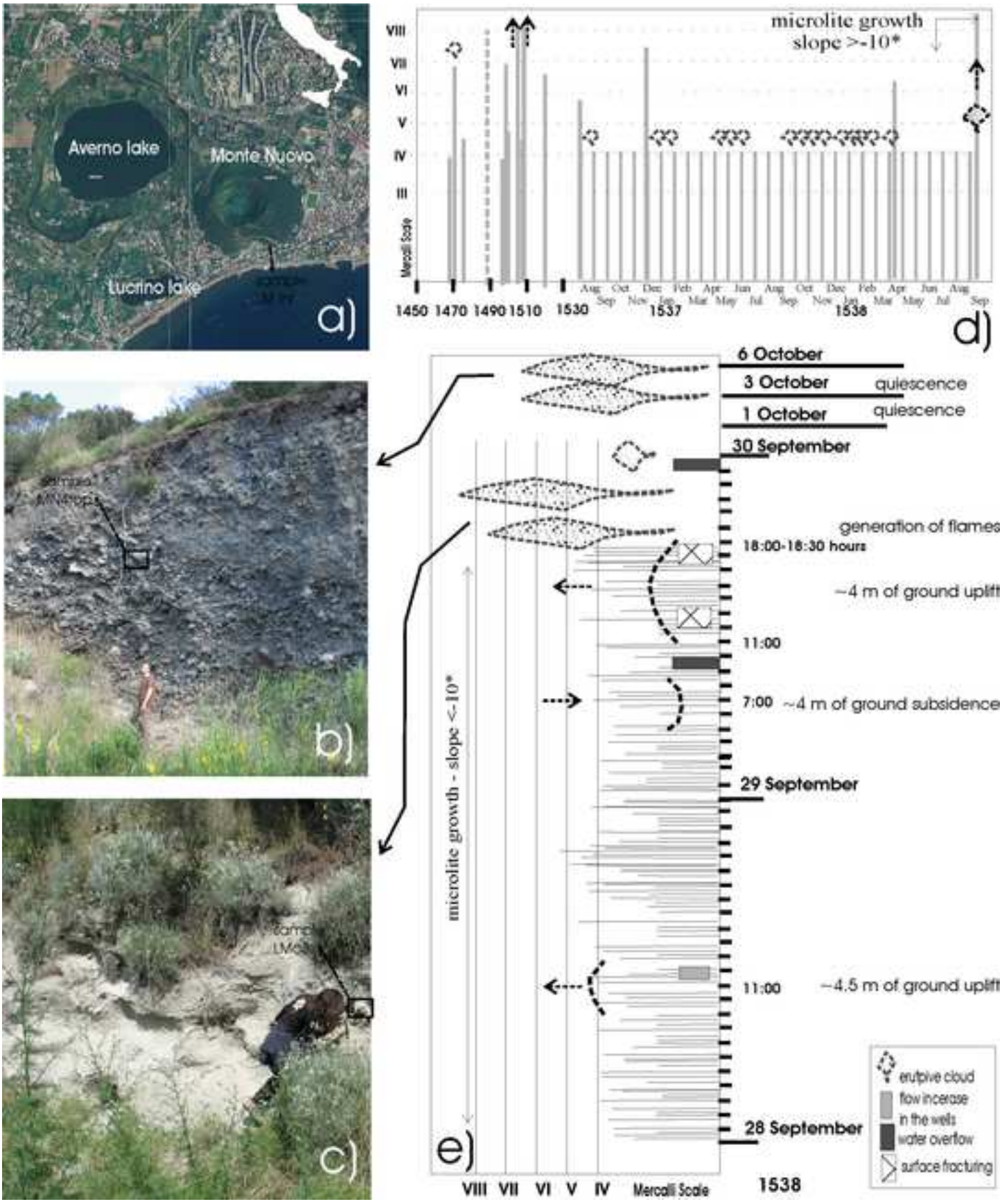

Figure 2

Click here to download Figure Figure_2.tif

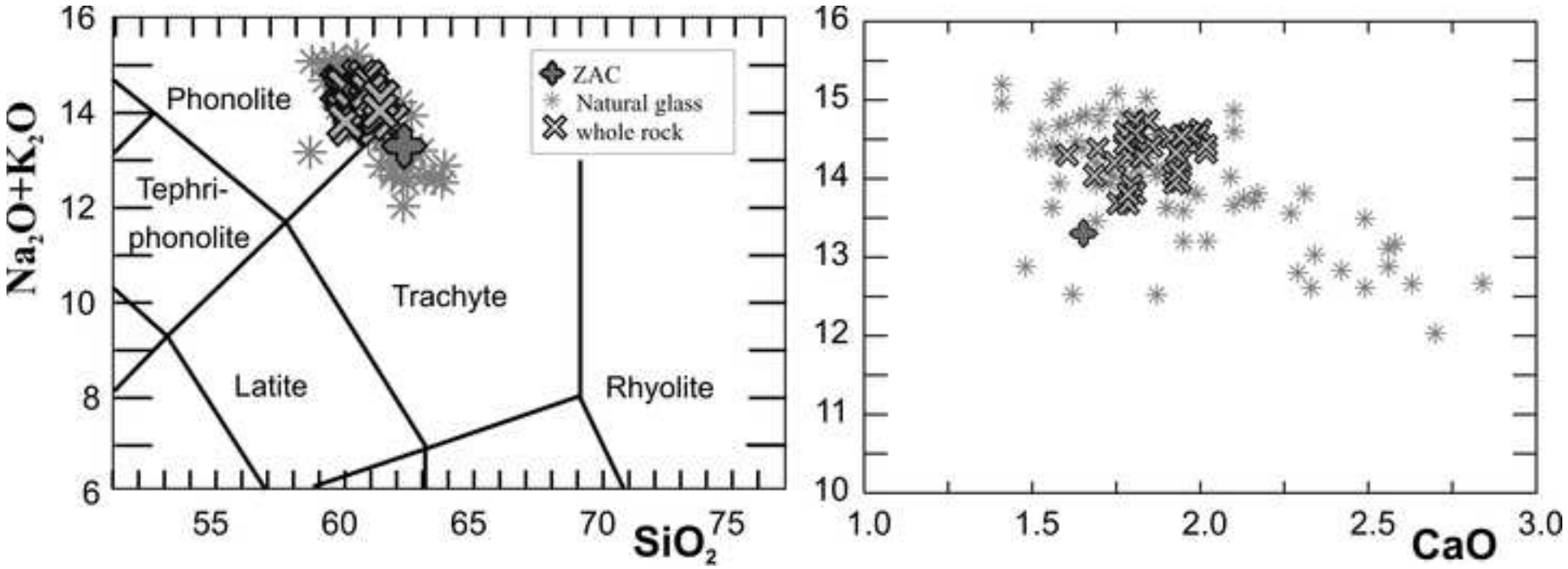

Figure 3

Click here to download Figure Figure_3.tif

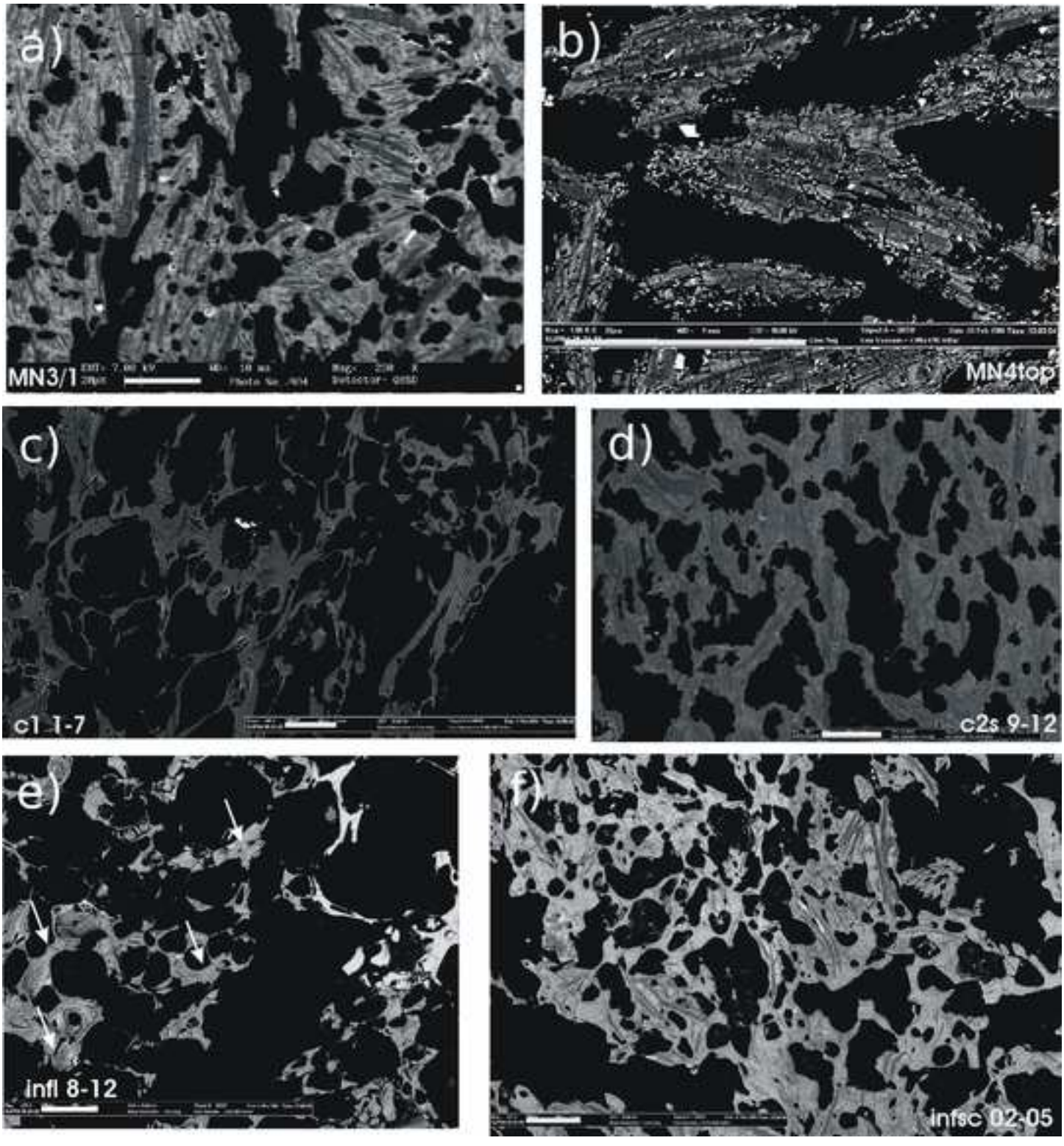

Figure 4

Click here to download Figure Figure_4.tif

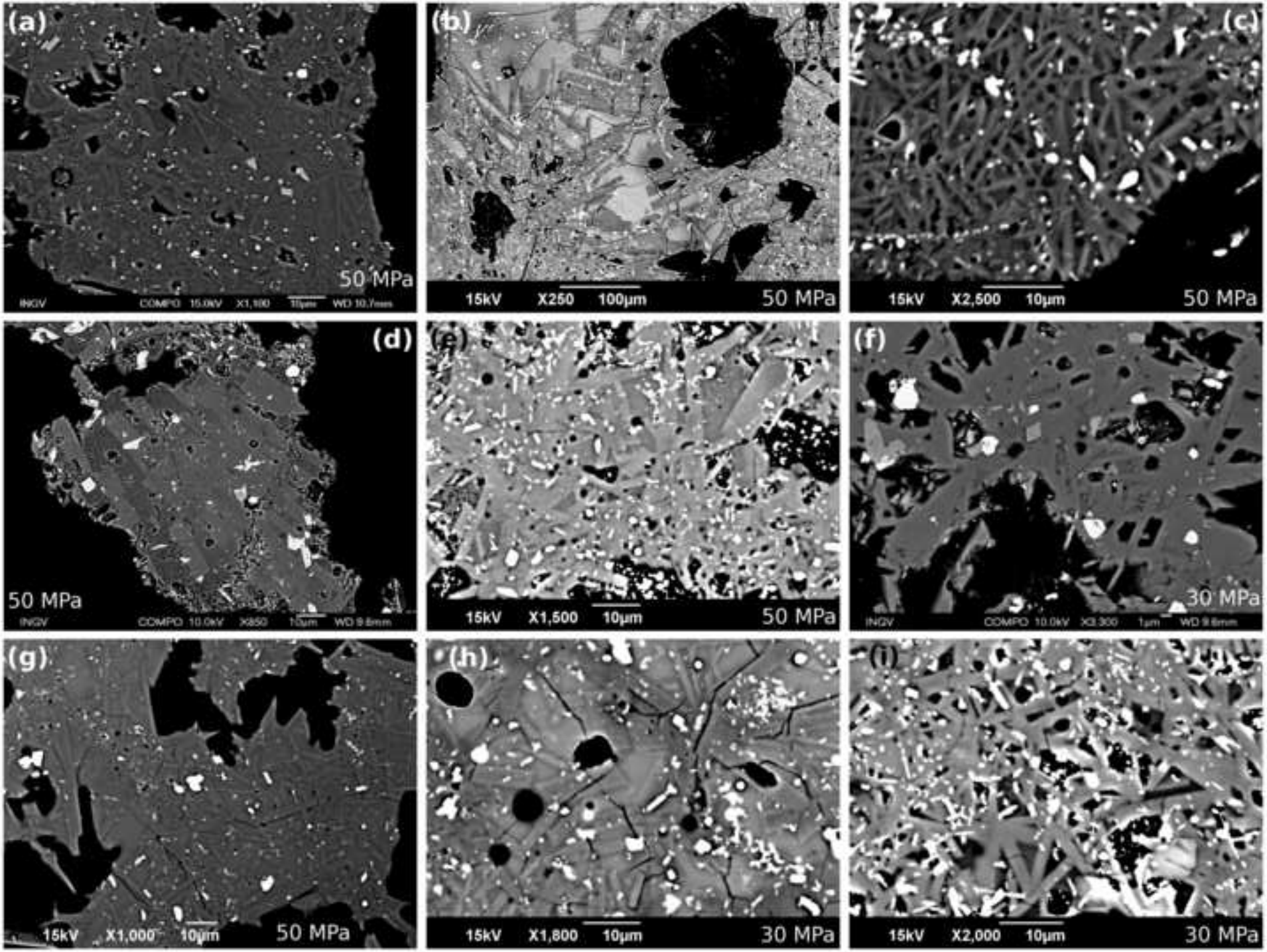

Figure 5

Click here to download Figure Figure_5.tif

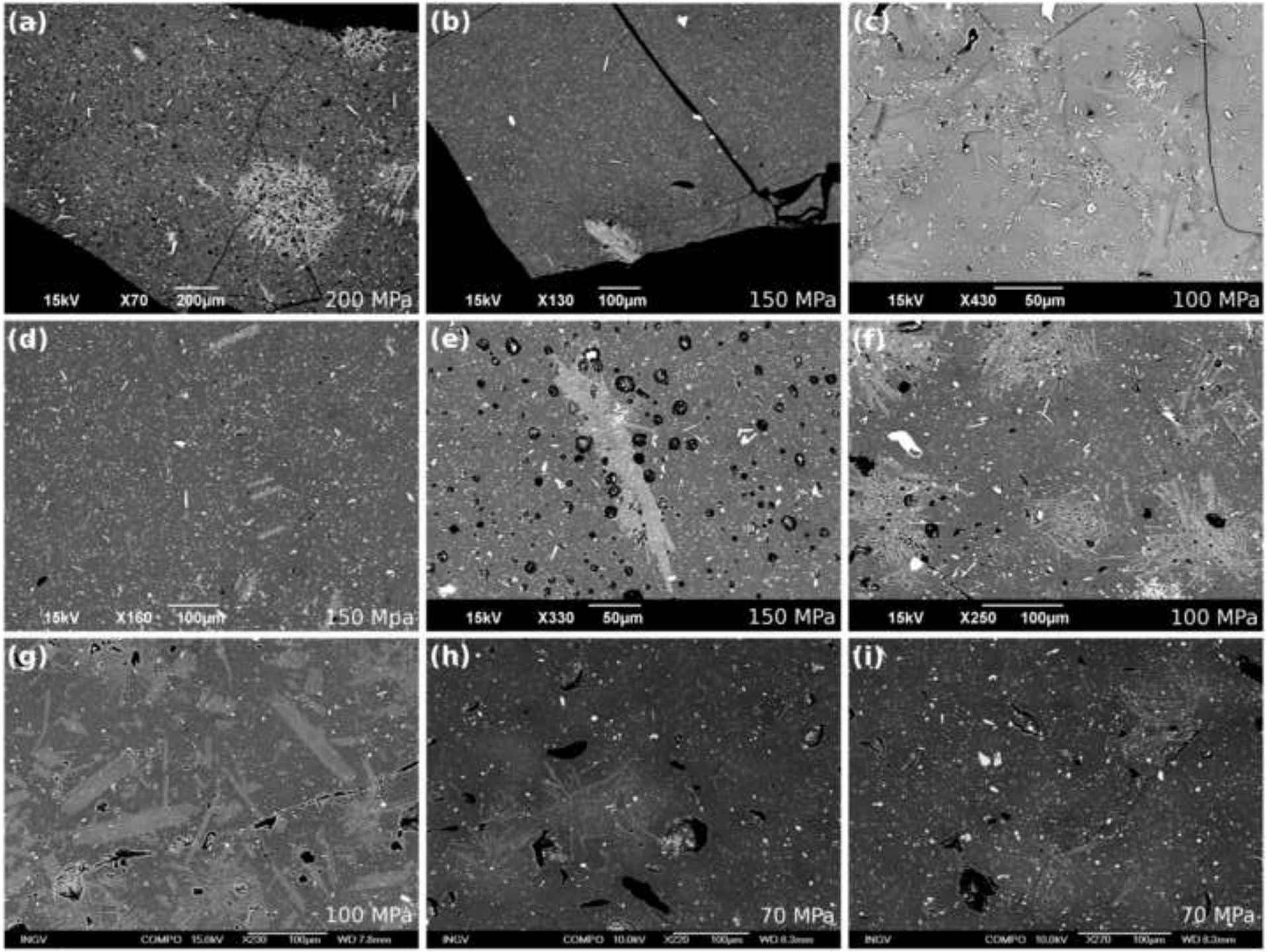

Figure 6

Click here to download Figure Figure_6.tif

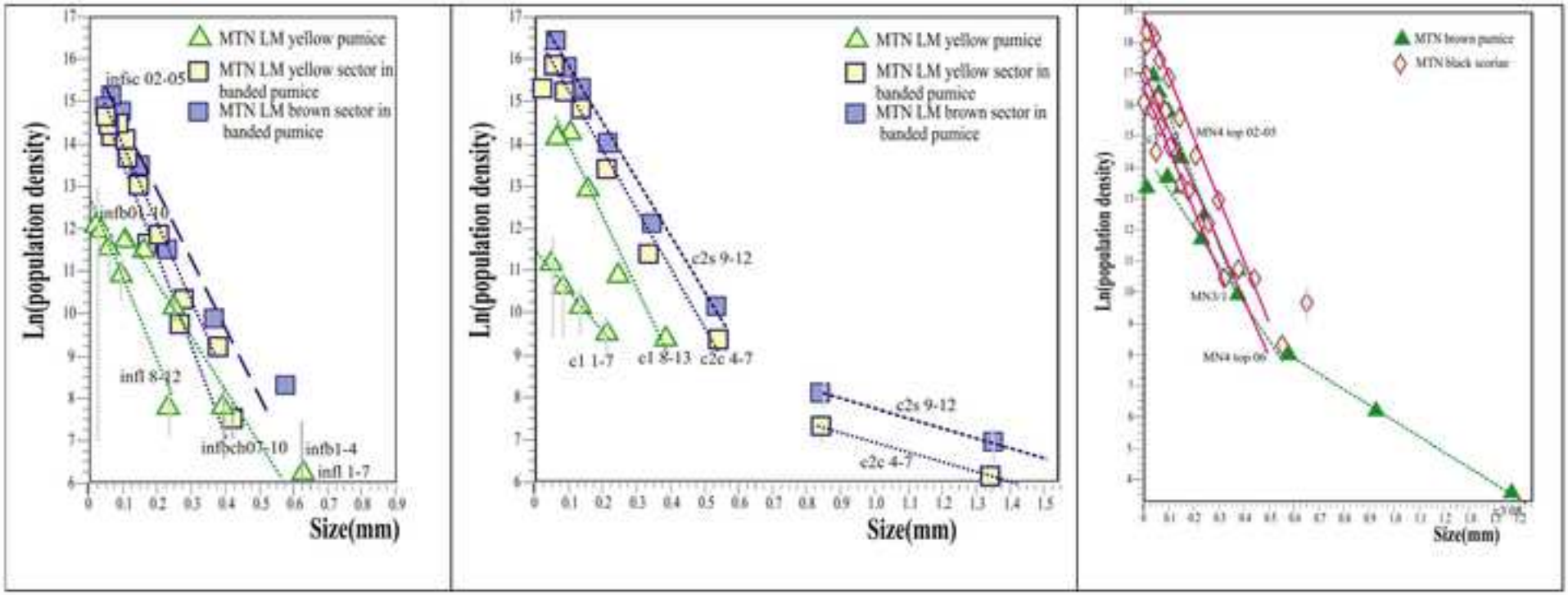

Figure 7

Click here to download Figure Figure_7.tif

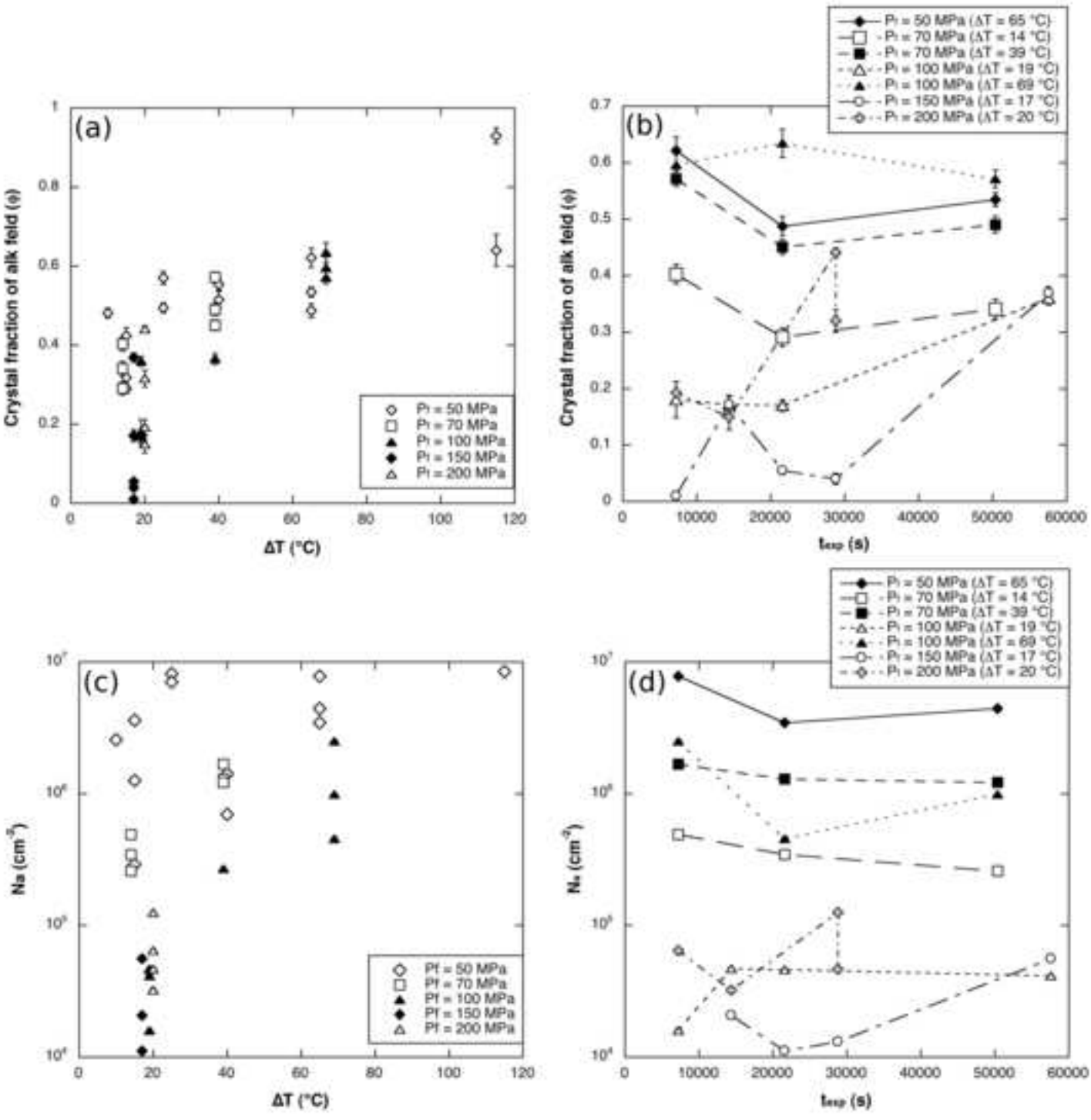

Figure 8

Click here to download Figure Figure_8.tif

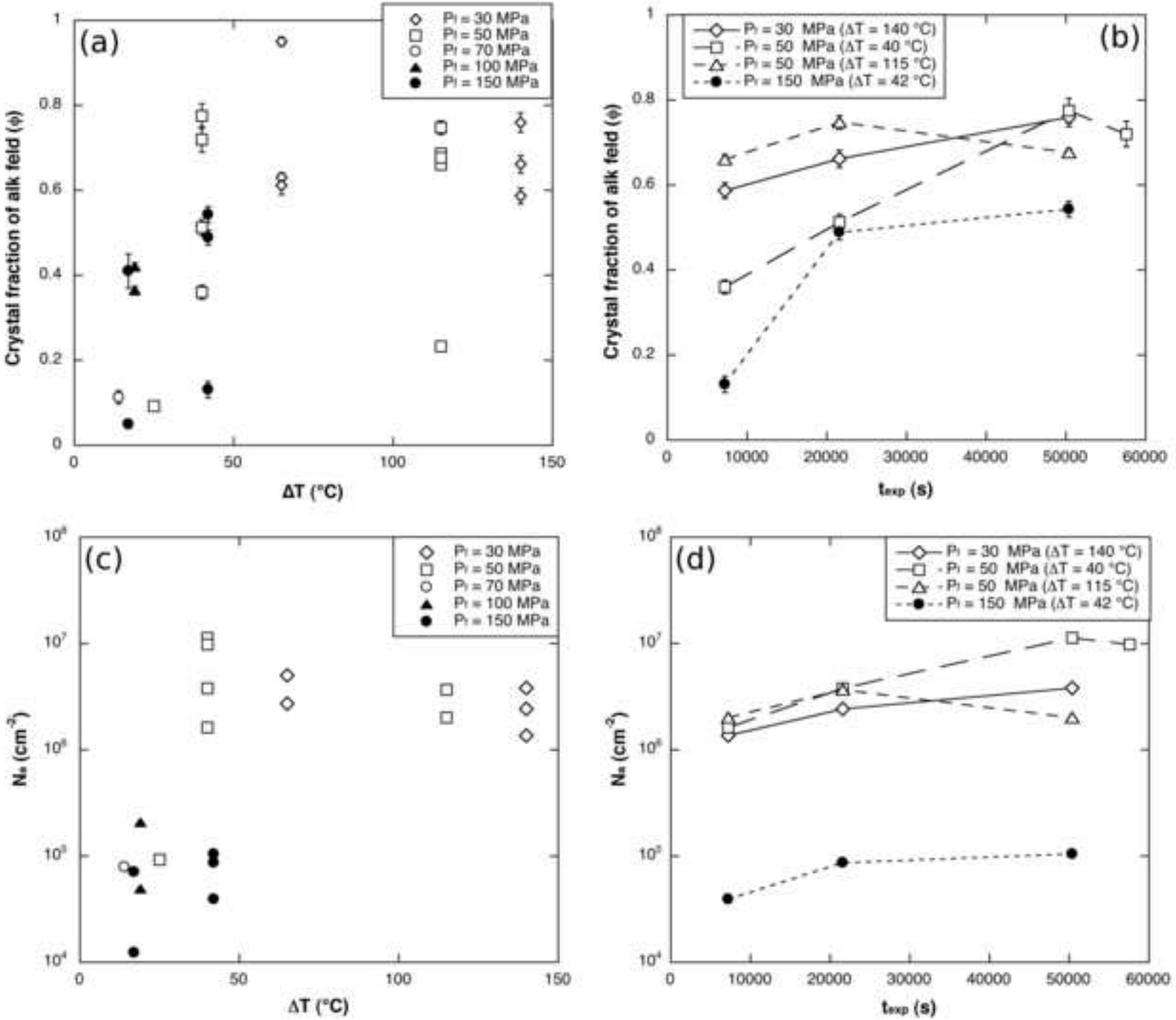

Figure 9

Click here to download Figure Figure_9.tif

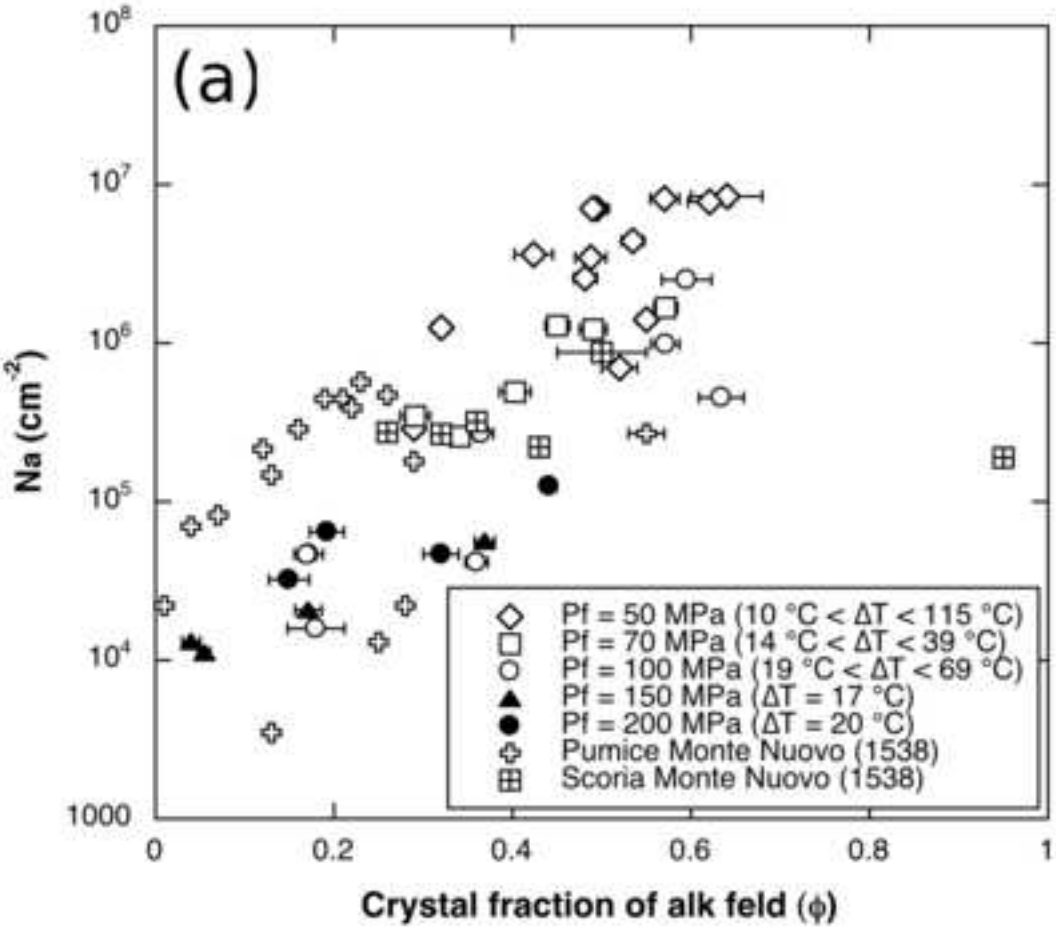

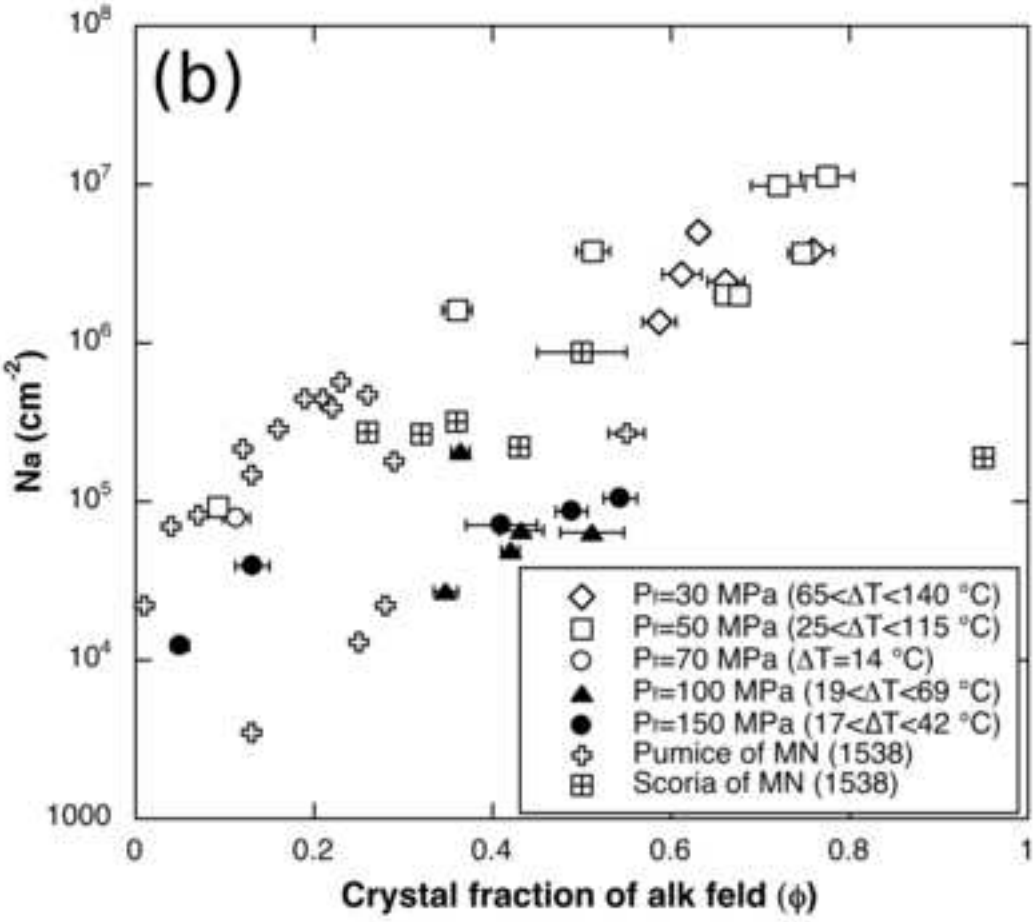

Table 1: Chemical composition of ZAC (from Di Matteo et al. 2004) and average for natural samples from units selected for this study (see Piochi et al., 2008 for not H_2O-free normalized data). FeO* = total iron as FeO.

oxide (wt%)	**ZAC**	**LM inf**	**LMc**	**MN4**
SiO_2	62.18	60.76	60.77	63.71
TiO_2	0.45	0.42	0.43	0.31
Al_2O_3	18.70	19.09	19.39	19.91
FeO*	3.19	3.05	3.05	1.63
MnO	0.27	0.27	0.27	0.07
MgO	0.23	0.23	0.24	0.12
CaO	1.65	1.89	1.94	1.55
Na_2O	6.16	7.09	6.82	6.67
K_2O	7.14	7.17	7.08	6.04
P_2O_5	0.02	0.03	0.02	0.01
Total	100.00	100.00	100.00	100.00

Table 2

Table 2. Experimental conditions for "isothermal cooling", "decompression + cooling" and "isothermal decompression" experiments.

sample	T_i (°C)	T_f (°C)	P (MPa)	t_m (s)	t_{exp} (s)	*H_2O (wt. %)	ΔT (°C)	–ΔT (°C)
Isobaric cooling experiments								
D20	900	750	200	72000	28800	7	20	131
D15	900	775	150	7200	7200	6	17	108
D13	880	775	150	7200	28800	6	17	88
D6	880	800	100	7200	21600	5.2	19	61
D11	900	850	50	7200	7200	2.7	15	35
D12	900	850	50	7200	14400	2.7	15	35
D33	900	840	50	7200	14400	2.7	25	35
D10	900	825	50	7200	28800	2.7	40	35
D9	900	825	50	7200	57600	2.7	40	35
D69	880	750	50	7200	21600	2.7	115	15
D78	880	750	50	7200	50400	2.7	115	15

sample	T_i (°C)	T_f (°C)	P_i (MPa)	P_f (MPa)	t_m (s)	t_{exp} (s)	*H_2O (wt. %)	ΔT (°C)	–ΔT (°C)
Decompression + cooling experiments									
D17	825	775	200	150	72000	21600	6	17	56
D25	825	775	200	150	72000	57600	6	17	56
D29	825	800	200	100	7200	57600	5.2	19	56
D21	825	825	200	50	7200	57600	2.7	40	56
Isothermal decompression experiments									
D62	825	825	150	30	3600	50400	1.7	65	33

note: T_i = initial (or melting) temperature; T_f = final (or experimental) temperature; P_i = initial (or melting) pressure; P_f = final (or experimental) pressure; t_m = melting time; t_{exp} = experimental time; ΔT = the undercooling degree; -ΔT = the superheating degree. *H_2O (wt %) was calculated using the polynomial fit by Di Matteo et al. (2004).

Table 3. Experimental results of nucleation and growth of alkali feldspar during “isothermal cooling”, “decompression + cooling” and “isothermal decompression” experiments.

sample	Na (cm^{-2})	ϕ	L (cm)	Y_L (cm/s)	phases
Isobaric cooling experiments					
D20	4.6E+04(1)	0.32(0.02)	0.0260(0.0095)	4.5E-07(9)	gl-af-cpx-mt-bt-bl
D15	n.d.	0.01	n.d.	n.d.	gl-af-cpx-mt-bt-bl
D13	1.31E+04(1)	0.04(0.01)	0.0116(0.0020)	2.0E-07(4)	gl-af-cpx-mt-bt-bl
D6	4.62E+04(1)	0.17(0.01)	0.0182(0.0032)	2.8E-07(4)	gl-af-cpx-mt-bl
D11	2.90E+05(4)	0.29(0.01)	0.0107(0.0035)	7.4E-07(2)	gl-af-cpx-mt-bl
D12	1.26E+06(1)	0.32(0.01)	0.0096(0.0019)	3.3E-07(7)	gl-af-cpx-mt-bl
D33	7.1E+06(1)	0.49(0.01)	0.0041(0.0006)	1.4E-07(2)	af-cpx-mt-gl-bl
D10	6.97E+05(2)	0.52(0.02)	0.0116(0.0020)	2.0E-07(3)	af-cpx-mt-gl-bl
D9	1.41E+06(2)	0.55(0.01)	0.0045(0.0011)	3.9E-08(9)	af-cpx-mt-gl-bl
D69	n.d.	0.93(0.02)	n.d.	n.d.	af-cpx-mt-gl-bl-sod
D78	n.d.	0.93(0.02)	n.d.	n.d.	af-cpx-mt-gl-bl-sod
Decompression + cooling experiments					
D17	1.23E+04(1)	0.05(0.01)	0.0092(0.0022)	2.13E-07(8)	gl-af-cpx-mt-bt-bl
D25	7.11E+04(6)	0.41(0.04)	0.0174(0.0032)	1.51E-07(3)	gl-af-cpx-mt-bt-bl
D29	4.92E+04(5)	0.42(0.01)	0.0185(0.003)	1.6E-07(3)	gl-af-cpx-mt-bl
D21	9.82E+06(3)	0.72(0.03)	0.004(0.0012)	3.5E+08(2)	af-cpx-mt-gl-bl
Isothermal decompression experiments					
D62	n.d.	0.95(0.01)	n.d.	n.d.	af-cpx-mt-gl-bl-sod

note: N_a = nucleation density; ϕ = volume fraction; L = maximum length; Y_L = maximum growth rate. The value in parentheses is the standard deviation of the mean value. n.d. = not determined phases presents because the contrast between several phases is not sufficient to distinguish them in BSE images.

Table 4: Mineral phase abundances (wt%) in the Monte Nuovo products as determined by semi-quantitative analyses of the XRPD data (see Supplementary Material 2).

sample	Anorthoclase	Sanidine	Sodalite	Biotite	Magnetite
LM C3 wr	70.9	24.8	3.4	0.6	0.4
LM C3 sh	82.6	14.2	2.8	0.2	0.3
LM inf l wr	35.9	63.7	-	0.5	-
LM inf l sh	34.9	64.9	-	0.2	-
LM inf d sh	39.8	59.6	-	0.5	0.1
MN4wr	59.5	33.6	5.8	-	1.1
MN4 sh	54.9	39.2	5.6	-	0.3

Note: Goodness of Fitt (GOF) <3; refer to text for analytical procedures; XRPD patterns and crystallographic index phase in the Supplementary Material 2.

Table 5

Table 5: Crystal growth rates (Y_L) as derived by experiments and related residence time (t_r) as calculated through the equation: $t_r = (-1/Y_L * \text{slope})$. Slopes are from the CSD diagrams in Fig. 7.

sample	**slope**	**intercept (mm)**	**tr (h) - *mean***	**tr (h) - *min***	**tr (h) - *max***	**tr(days) - *max***
infl 8-12	-20.8	12.8	6.1	1.1	121.6	5.1
infb 01-10	-21.6	15.7	5.8	1.1	117.2	4.9
infl 1-7	-12.3	13.2	10.2	1.9	204.8	8.5
infb 1-4	-15.6	16.2	8.0	1.5	161.7	6.7
infsc 02-05	-18.5	16.0	6.8	1.3	136.4	5.7
infb ch07-10	-16.1	13.3	7.8	1.4	156.5	6.5
c1 1-7	-9.7	11.3	13.0	2.4	261.1	10.9
c1 8-13	-17.0	15.8	7.4	1.4	148.9	6.2
c2c 4-7 - 1	-2.3	9.3	54.7	10.1	1099.5	45.8
c2s 9-12 - 1	-2.3	10.0	55.6	10.2	1117.4	46.6
c2c 4-7 - 2	-8.1	16.8	15.6	2.9	313.2	13.1
c2s 9-12 - 2	-13.7	17.3	9.2	1.7	184.4	7.7
MN4 top 06 - 1	-6.7	11.0	18.9	3.5	378.8	15.8
MN4 top 06 - 2	-12.9	14.7	9.7	1.8	195.1	8.1
c3 1-2	-19.6	16.3	6.4	1.2	128.6	5.4
c3 1-2	-20.4	17.5	6.2	1.1	123.7	5.2
MN4top 02-05	-20.0	19.0	6.3	1.2	126.3	5.3
Experimental Growth rate			*mean Y_L =*	*mean Y_L =*	*mean Y_L =*	
		cm/s	*2.21E-07*	*1.20E-06*	*1.10E-08*	
		mm/h	*7.96E-03*	*4.32E-02*	*3.96E-04*	